AN ANALYSIS OF PERL MAGNETIC RESONANCE IMAGING

THEORY AND IMPLEMENTATION

A Senior Honors Thesis

by

MARK CHRISTIAN KREMKUS

Submitted to the Office of Honors Programs
& Academic Scholarships
Texas A&M University
in partial fulfillment for the designation of

UNIVERSITY UNDERGRADUATE
RESEARCH FELLOW

Approved as to style and content by:

Steven M. Wright
(Fellows Advisor)

Edward A. Funkhouser
(Executive Director)

April 2001

Group: Engineering

AN ANALYSIS OF PERL MAGNETIC RESONANCE IMAGING THEORY AND IMPLEMENTATION

A Senior Honors Thesis

by

MARK CHRISTIAN KREMKUS

Submitted to the Office of Honors Programs
& Academic Scholarships
Texas A&M University
in partial fulfillment of the requirements of the

UNIVERSITY UNDERGRADUATE
RESEARCH FELLOWS

April 2001

Group: Engineering

ABSTRACT

An Analysis of PERL Magnetic Resonance Imaging

Theory and Implementation. (April 2001)

Mark Kremkus
Department of Electrical Engineering
Texas A&M University

Fellows Advisor: Dr. Steven Wright
Department of Electrical Engineering

The goal of PERL MRI in its most basic form is single shot imaging without the need to rapidly switch gradients to encode spatial information into the signal. PERL MRI incorporates the application of the PERL field into the standard spin echo sequence following the excitation of spins, creating an initial phase pattern that causes echoes to form in the signal in the presence of a constant readout gradient. The echo train that occurs can be sampled and decoded into image data using reconstruction methods that are not discussed in this paper.

The theoretical analysis of PERL MRI that will be discussed verifies the mathematical basis for the formation of a periodic signal resulting from cyclical coherence of the spins within a homogeneous sample. Theory also indicates a significant reduction in the maximum amount of coherence present in the PERL signal as compared to total coherence that occurs at the center of k-space, indicating that SNR may suffer with this technique.

The effects of specific design parameters on the field generated by a proposed PERL coil design layout is discussed, and an experimental design is presented. The experimental PERL coil produces an approximation of the PERL field over a limited spatial region at the center of the coil structure.

The PERL MRI pulse sequence was implemented by interfacing the experimental PERL coils to the slice selection gradient channel of a TecMag MRI console. Experiments were conducted using water phantom with varying amounts of PERL prephasing and readout gradient strengths, in an attempt to obtain data confirming the effects of the PERL imaging parameters on the PERL signal.

These experiments were inconclusive as to the formation of a PERL echo train, but some form of cyclical coherence appeared to result. The evidence does not suggest that the PERL approach is robust when implemented with the experimental apparatus used in these experiments. Additional experiments are proposed, and possible explanations for the non-ideality of the experimental results are presented.

ACKNOWLEDGMENTS

I wish to thank the following people for their contributions to this project:

- David Brown, for assistance with Matlab code, RF coil tuning, and finding things around the lab.
- Mary McDougal, who believes that I possess adequate intelligence to study MRI in graduate school.
- David Spence, for attempting to make my linear gradient coils work.
- Dan Spence, for his extensive help with running the TecMag system, the long hours spent with me in the laboratory to investigate PERL, and his knowledge and expertise in physics and MRI.
- Dr. Steven Wright, whose thought-provoking teaching techniques and curiosity inspired me to undertake this project.

TABLE OF CONTENTS

Page

ABSTRACT iii

ACKNOWLEDGMENTS iv

TABLE OF CONTENTS v

LIST OF FIGURES vi

INTRODUCTION 1

PERL MRI THEORY 3

- Echo Spacing and Resolution in x 4
- Resolution in y 7
- Maximum PERL Echo Amplitude 8
- A Simplified Approximation of the PERL Signal 9

PERL COIL LAYOUT AND DESIGN PARAMETERS 12

- Layout 12
- Design Parameters Affecting Performance Along *x* 14
- Design Parameters Affecting Performance Along *y* 20

METHODS 24

- PERL Coil Modeling and Construction 24
- Experimentation 27

RESULTS AND DISCUSSION 29

CONCLUSIONS 30

REFERENCES 32

APPENDIX A - FUNDAMENTALS OF MRI 33

- Resolution and Field of View 41
- Contrast 42
- Radio-frequency Coils 44
- Gradient Coils 45

APPENDIX B - BURST IMAGING 47

- Limitations of BURST 53

VITA 55

LIST OF FIGURES

Page

Figure 1.0 The PERL Field ... 2

Figure 2.0 Basic PERL Pulse Diagram ... 3

Figure 2.1 S(t) for $N=2$ ... 11

Figure 2.2 S(t) for $N=6$ ... 11

Figure 3.0 Sinusoidal Field ... 12

Figure 3.1 The Basic PERL Coil Layout ... 14

Figure 3.2 Field along x in Imaging Region for $N=5$ ... 15

Figure 3.3 Field along x in Imaging Region for $N=6$ ... 16

Figure 3.4 Field along x in Imaging Region for $N=100$ ... 16

Figure 3.5 Field Strength vs. L ... 18

Figure 3.6 Field Pattern Along x for $N=5$ and $d / \lambda << 1$ ... 19

Figure 3.7 Field Pattern Along x for $N=5$ and $d / \lambda > 1$ ... 19

Figure 3.8 Field Pattern Along x for $N=10$ and $s / \lambda > 1$ ... 20

Figure 3.9a Effect of d on Gradient strength and Linear Region Along the y axis ... 21

Figure 3.9b Effect of d on Gradient strength and Linear Region Along the y axis ... 22

Figure 3.10 Effect of Varying s / λ on the Derivative of the Field ... 23

Figure 4.0 Experimental PERL Coil Design ... 24

Figure 4.1 Simulated PERL Field Generated by Experimental Coil ... 25

Figure 4.2 The PERL Field on the y axis ... 26

Figure 4.3 The Derivative of the PERL Field on the y axis ... 26

Figure 4.4 Periodicity of the PERL Field ... 27

INTRODUCTION

Current MRI research seeks to extend the capability of clinical MRI to the realm of dynamic, real-time imaging. PERL MRI, originally theorized by Dr. Samuel Patz and company of the Harvard School of Medicine, represents a departure from conventional MRI techniques, which suffer from speed limitations imposed by the rapid switching of magnetic fields. Eliminating the penalties associated with high frequency field switching is the motivation behind the PERL technique, which may have the potential to create images with a fundamentally new encoding scheme. In essence, PERL MRI attempts to trade the difficulties and limitations of the magnetic field switching employed by conventional methods for a more complex mathematical encoding scheme combined with a reduction in signal to noise.

Ultra-fast imaging techniques rely on rapidly switching magnetic field gradients to encode spatial information into the time-varying signal that is emitted by the object being imaged. Faster switching of magnetic field gradients allows the sampling rate to increase, and subsequently yields high resolution images in a relatively short amount of time. If a magnetic field shifts too rapidly, however, it can induce currents in the object being imaged, which results in burning of tissue as well as nerve stimulation. This places a lower limit on image acquisition time that can only be circumvented by encoding the signal quickly by another means. PERL MRI creates a phase map prior to data acquisition, and can potentially encode all spatial information with this single application, facilitating imaging without the need for rapidly switching the field direction.

PERL MRI encodes spatial information into the MRI signal using a magnetic field to pre-phase the spins within the sample. This magnetic field, known as the PERL field, is PERiodic in x and Linear in y, and is given by [1]:

$$B_z(x, y) = g_y y \cos(q_x x). \tag{1.0}$$

Figure 1.0 depicts the PERL field graphically.

This thesis follows the style and format of the *Institute of Electrical and Electronics Engineers* in all aspects except those set by the University Undergraduate Research Fellows of Texas A&M University.

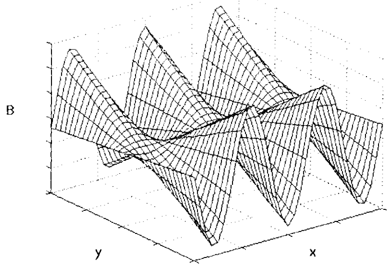

Figure 1.0 The PERL Field

Due to the nonlinearity of this field, the mathematical reconstruction of the image from the time domain departs from the standard reconstruction method. Instead of using the Fourier transform on both dimensions, only the x dimension is converted from the time domain using the Fourier transform, while the y dimension is reconstructed from the solution to a Bessel function integral transform, as described in a related paper [2].

This paper primarily explores the relationship between formation of echoes and the state of the spins within a homogeneous sample, and thus identifies the origins of the echo train and applies this knowledge to investigate the feasibility of the PERL approach. Theoretical models were used to yield the echo train formed by a homogeneous phantom, and a close approximation of the actual signal was then developed using a relatively simple relation. Also presented is the effect of PERL coil layout parameters on the PERL field in a limited spatial region, and the significant design tradeoffs and considerations that occur in building an experimental PERL coil. Finally, experiments were conducted using the experimental PERL coil and two variations of the basic PERL sequence to verify the formation of the echo train in the presence of real world non-idealities.

PERL MRI THEORY

The basic pulse sequence proposed by Patz and company in [1] and [2] consists of the application of the PERL field to prephase the spins in the sample prior to the 180° pulse in the spin echo sequence, and is shown in Figure 2.0.

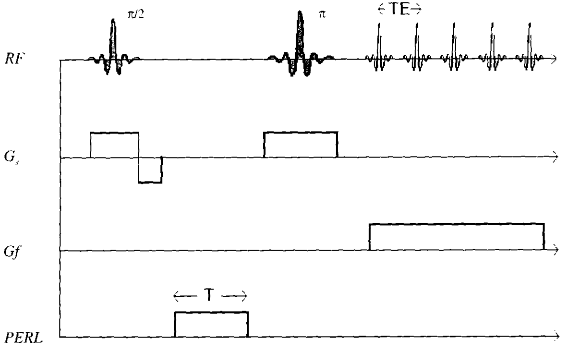

Figure 2.0 Basic PERL Pulse Diagram

The sequence begins with a π/2 slice selective excitation pulse followed by a refocusing that centers the spins in k-space. The PERL field is then applied for a duration of T on the channel normally used by the phase encode gradients, causing a phase shift given by:

$$\theta(x, y) = \gamma g_y yT\cos(q_x x). \tag{2.0}$$

Data acquisition occurs by sampling an echo train during the readout gradient, G_f, where each echo is separated in time by TE. Since the π pulse inverts the sign of the phase, the phase map during data acquisition becomes:

$$\theta(x, y, t) = \gamma G_x xt - \gamma g_y yT\cos(q_x x). \tag{2.1}$$

The signal that results represents the contributions from all of the spins in the field-of-view, or FOV, at a given point in time measured from the beginning of the application of the readout gradient:

$$S(t) = \iint \rho(x, y) e^{j\gamma\left(G_x xt - \gamma g_y T\cos(q_x x)\right)} dxdy \ . \tag{2.2}$$

In (2.2), relaxation losses associated with spin-spin and spin-lattice relaxation are included within the spin density term, $\rho(x, y)$, which will be set equal to unity for the remainder of this discussion, representing a homogeneous sample experiencing no relaxation losses.

Echo Spacing and Resolution in x

The parameter TE governs the inter-echo spacing and hence represents a crucial parameter in implementing PERL MRI. By manipulating (2.2) for two different cases, a relation for the echo time can be obtained. For *case a*, (2.2) is integrated over the interval y = 0 ... b , yielding:

$$S(t) = \int \frac{j\left(e^{-jb\gamma g_y T\cos(q_x x)} - 1\right)}{\gamma g_y T\cos(q_x x)} e^{j\gamma G_x xt} dx. \tag{2.3a}$$

For *case b*, integrating (2.2) over the interval y = - b ... b yields:

$$S(t) = \int \frac{j}{\gamma g_y T\cos(q_x x)} \left(e^{-jb\gamma g_y T\cos(q_x x)} - e^{jb\gamma g_y T\cos(q_x x)}\right) e^{j\gamma G_x xt} dx. \tag{2.3b}$$

The Jacobi-Anger expansion [1]:

$$e^{jA\cos B} = \sum_{m=-\infty}^{\infty} j^{m} J_{m}(A) e^{jmB}, \tag{2.4}$$

$$J_m(A) = \sum_{k=0}^{\infty} \frac{(-1)^k \left(\frac{A}{2}\right)^{m+2k}}{k!(k+m)!}, \tag{2.5}$$

from which it is clear that:

$$\begin{aligned} J_m(A) &= J_m(-A), && m \text{ even}, \\ J_m(A) &= -J_m(-A), && m \text{ odd}, \end{aligned} \tag{2.6}$$

provides a useful tool in analyzing the periodicity of the signal. Substituting (2.4) into (2.3a) yields:

$$S(t) = \int \frac{1}{\gamma g_y T \cos(q_x x)} \left(\sum_{m=-\infty}^{\infty} j^{m+1} J_m(\gamma b g_y T) e^{jmq_x x} - 1 \right) e^{j\gamma G_x x t} dx. \tag{2.7a}$$

Substituting (2.4) into (2.3b) gives:

$$S(t) = \int \frac{1}{\gamma g_y T \cos(q_x x)} \left(\sum_{m=-\infty}^{\infty} j^{m+1} \left[J_m(-\gamma b g_y T) - J_m(\gamma b g_y T) \right] e^{jmq_x x} \right) e^{j\gamma G_x x t} dx. \tag{2.7b}$$

All terms in equation (2.7a) contribute to the signal, while the terms in equation (2.7b) become zero when m is even. Since (2.7b) can be completely represented by odd values of m, the terms in its sum are always real and alternate in sign with each echo. Both signals consist of a series of m echoes, each of which reaches a relative maximum or minimum when the dependence on x is minimized, which occurs when the phase of a term within the sum becomes zero [1]:

$$TE_m = \frac{mq_x}{\gamma G_x}. \tag{2.8}$$

The echo times, TE_m, occur when there is a peak in the signal, and the time between them gives the period of the magnitude of the signal. Since $\Delta m = 1$ in *case a*, (2.8) can be modified to give [1]:

$$\Delta TE = \frac{q_x}{\gamma G_x}. \tag{2.9a}$$

In *case b*, only the odd values of m contribute to the echo train, meaning $\Delta m = 2$ and:

$$\Delta TE = \frac{2q_x}{\gamma G_x}. \tag{2.9b}$$

In both cases, the period of the signal is:

$$\Delta T = \frac{4q_x}{\gamma G_x}. \tag{2.10}$$

Considering the more realistic case in which the sample is neither wholly within half of the PERL field nor balanced exactly in the PERL field, (2.7b) becomes:

$$S(t) = \int \frac{1}{\gamma g_y T \cos(q_x x)} \left(\sum_{m=-\infty}^{\infty} j^{m+1} \left[J_m(-\gamma b_1 g_y T) - J_m(\gamma b_2 g_y T) \right] e^{jmq_x x} \right) e^{j\gamma G_x xt} dx. \tag{2.11}$$

In this case, the terms in the sum will still interfere destructively when m is even and constructively when m is odd, and the signal will consist of two alternating echo trains of differing amplitude, each with a *ΔTE* given by (2.9b).

The analysis concerning resolution in x given by Patz and company in [1] is included here for completeness, and is extended to include the cases discussed previously. The Nyquist criterion states that the maximum measurable frequency in the time-varying signal is equal to the data sampling rate if two measurements are made in quadrature at each sampling time. Since the dwell time, *DW*, is the inverse of the sampling rate, the Nyquist criterion can be stated as :

$$\gamma G_x x_{res} N \cdot DW = 2\pi \tag{2.12}$$

where N is the number of samples taken per echo and x_{res} is the resolution along the x axis[1]. The total sampling time per echo, $N\,DW$, will be equal to ΔTE, yielding:

$$\gamma G_x x_{res} \Delta TE = 2\pi. \tag{2.13}$$

Substituting (2.9a) into (2.13) and solving for x_{res} gives:

$$x_{res} = \frac{2\pi}{q_x}. \tag{2.14}$$

This relation is true for all cases, regardless of the limits of integration along y, simply because it stems from the rephasing of spins as controlled by the periodicity of the PERL field. In other words, the fact that some echoes combine destructively, leading to a longer effective spacing between echoes, results from odd symmetry and does not increase the resolution in either half of the field.

Resolution in y

From the previous discussion concerning the formation of echoes, it became clear that the time-varying signal is periodic for a homogeneous, lossless phantom. If each echo were identical, then the formation of an echo train would not provide any additional information. The fact that we are dealing with a homogeneous phantom for simplicity hides the fact that the state of the spins in the sample is unique for every point in time. Since the echo train itself consists of contributions from every spin and is itself periodic for a homogeneous, lossless sample, this implies that the same combination of spins exist for every echo, but does not mean that the total spin state over the field-of-view is identical. Consider the phase given by (2.1) and repeated here:

$$\theta(x, y, t) = \gamma G_x x t - \gamma g_y y T \cos(q_x x). \tag{2.15}$$

We want to analyze the changes in the phase map itself over time. Taking the derivative of (2.15) with respect to x gives:

$$\frac{d\theta(x,y,t)}{dx} = \gamma G_x t + \gamma q_x g_y y T \sin(q_x x). \tag{2.16}$$

Evidently, a single maximum exists for a given value of x except for those values that cause $\sin(q_x x)$ to equal zero, at which the derivative with respect to x is a constant for all y. Setting (2.16) to zero and solving for y yields:

$$y = \frac{-G_x t}{g_y q_x T \sin(q_x x)}, x \neq \frac{n\pi}{q_x}. \tag{2.17}$$

Equation (2.17) shows that the point on y at which the slope of the phase with respect to x changes sign for a given x moves linearly with time. This means that any two points in the time-varying signal that are one period apart in time consist of an equal contribution from a point along y that is displaced by some amount, Δy, from its location during the previous echo. Substituting the expression for the time between echoes in (2.9a) into (2.17) gives:

$$\Delta y = \frac{1}{\gamma g_y T \sin(q_x x)}, x \neq \frac{n\pi}{q_x}. \tag{2.18}$$

The minimum of (2.18) occurs when $\sin(q_x x) = 1$, implying that the resolution in y is:

$$y_{res} = \frac{1}{\gamma g_y T}. \tag{2.19}$$

Maximum PERL Echo Amplitude

Since PERL MRI relies on prephasing the phantom during the standard spin echo pulse sequence, the signal coherence at the center of k-space during a normal imaging sequence will never occur during PERL imaging. Consequently, the maximum PERL echo amplitude will be a fraction of the maximum amplitude of the spins at the center of k-space. Naturally, this lack of coherence can significantly decrease the signal to noise ratio, and seriously threatens the practicality of PERL MRI. A rudimentary analysis of maximum coherence in the PERL signal originates with a different form of equation (2.3b), which applies to a homogeneous sample with no relaxation losses balanced across the x axis:

$$S(t) = \int_{-a}^{a} \frac{2 \sin\left(b \gamma g_y T \cos\left(q_x x\right)\right)}{\gamma g_y T \cos\left(q_x x\right)} e^{j\gamma G_x x t} dx \, . \qquad (2.20)$$

For simplicity, we consider this equation for the t=0, resulting in the maximum amplitude. The integral is difficult to evaluate, but clearly reduces to zero as the product $g_y T$ approaches infinity. As the PERL field approaches zero, the integral approaches $4ab$, implying that smaller values of $g_y T$ cause the spins to approach the center of k-space, which is intuitively obvious.

A Simplified Approximation of the PERL Signal

The idealized cases discussed previously indicate that the signal generated by PERL pulse sequence is periodic with period given in (2.10) and repeated here as a frequency:

$$f_0 = \frac{\gamma G_x}{4 q_x}. \qquad (2.21)$$

A good approximation of the PERL signal results from first expanding the signal into a Fourier series with fundamental frequency given by (2.21). The Fourier coefficients are derived from the inner product of a periodic signal and the complex exponential kernel function over an interval spanning a complete period of the signal

$$c_n = f_0 \int_{\alpha}^{\alpha + T_0} S(t) e^{-j 2 \pi n f_0 t} dt \, , \qquad (2.22)$$

where we choose $\alpha = -T_0/2$ to simplify the result, and substitute only the time-varying component of the PERL signal for $S(t)$:

$$c_n = f_0 \int_{-1/2 f_0}^{1/2 f_0} e^{jt(\gamma G_x x - 2\pi n f_0)} dt . \tag{2.23}$$

Evaluating (2.23) yields:

$$c_n = \text{sinc}\left(\frac{2xq_x}{\pi} - n \right), \tag{2.24a}$$

where

$$\text{sinc}(A) = \frac{\sin(\pi A)}{\pi A}. \tag{2.24b}$$

The Fourier series representation of the PERL signal over an unbounded FOV then becomes:

$$S(t) = \iint e^{-j\gamma g_x yT \cos(q_x x)} \left(\sum_{n=-\infty}^{\infty} \text{sinc}\left(\frac{2xq_x}{\pi} - n \right) e^{-j2\pi n f_0 t} \right) dxdy \tag{2.25}$$

As n increments, it advances the center of the nth sinc function by $n\pi/2q_x$, which should not exceed the limits of integration on x at the maximum and minimum values of n. If the limits of integration on x can be expressed by $N\pi/2q_x$, where N is the maximum value of n, the signal is well approximated by:

$$S(t) \cong \int \int_{-a}^{a} e^{-j\gamma g_x yT \cos(q_x x)} \left(\sum_{k=1-2aq_x/\pi}^{2aq_x/\pi} e^{-j2(2k-1)\pi f_0 t} \right) dxdy . \tag{2.26}$$

This relation illustrates that the number of lobes in one period of the magnitude of the time-varying signal is equal to $2N$. As the limits of integration on x increase, the frequencies included in the signal increase, and the period width of the lobes within one period of the signal must decrease with the inverse of the maximum frequency. Figure 2.1 depicts the magnitude of the signal in (2.26) for $N=2$ which contrasts with the case when $N=6$ shown in Figure 2.2.

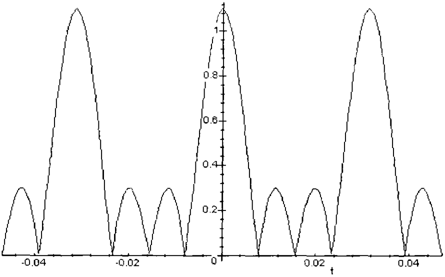

Figure 2.1 S(t) for N=2

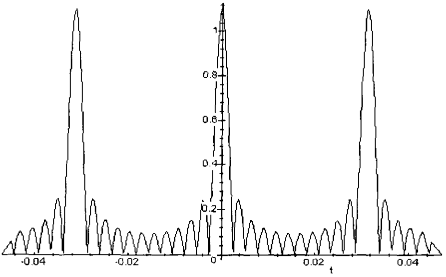

Figure 2.2 S(t) for N=6

PERL COIL LAYOUT AND DESIGN PARAMETERS

The mathematical simplicity of the PERL field itself does not extend to the physical implementation. The experimental coils designed and built for verifying the performance of PERL imaging approximate the PERL field well over the desired region of space, however, a number of considerations must be addressed with regard to implementing the PERL field over larger volumes. Also, the experimental coils image a small volume relative to the total volume occupied by the coils themselves, which is undesirable since space within the magnet bore is at a premium.

In this section, we discuss the relationships between the design parameters and the coil performance by conveying the rationale behind the general layout and outlining the tradeoffs in optimizing various aspects of the field, with an emphasis on strategies to reduce undesirable interdependence between parameters. Like all good coil designs, carefully designed PERL coils should minimize consumption of both space and current while maximizing field of view and gradient strength.

Layout

The periodic variation of the PERL field implies the use of alternating current elements, which create a perfect sinusoidal transverse field in the plane that contains the current elements, assuming that the elements extend infinitely in either direction. Figure 3.0 illustrates the phase relationship between currents and field, which is a perfect sinusoidal z-directed field in the plane of the current elements:

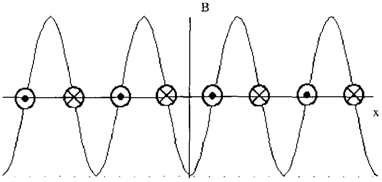

Figure 3.0 Sinusoidal Field

The amplitude of the periodic field deteriorates away from the plane containing the current elements rapidly due to both the usual field falloff with the inverse of the distance squared, as well the increasing cancellation of field vectors associated with adjacent elements as the distance from the pair increases. This effect severely limits the intensity of the field away from the source currents, particularly when the period of the sinusoid is small compared to the distance.

By using an identical current array displaced along the transverse axis, the field directly between the two planes doubles in amplitude. This does nothing, however, to induce uniformity along the transverse axis. The amplitude of the sinusoid increases greatly moving toward either current sheet. While this variation compromises the homogeneity of the amplitude of the field, the integrity of the sinusoid remains constant between the current sheets. The experimental coil does not include any layout features to decrease the variability along the transverse axis.

The layout must incorporate additional fixtures to implement the linear variation along the y axis. I achieve this by juxtaposing an identical set of current sheets symmetrically across the x axis, while displacing them by half a period along x so that the phase of the wires reverses moving across the x axis. The layout then enforces the condition that the phase of the sinusoid must reverse between the extremities of the field-of-view along y, but does not determine the nature of the field variation along y. The behavior of the field along y must intuitively include a region that exhibits good linearity. The extent of the linear region must then stem from the choice of the layout parameters d, s, and L, as shown in Figure 3.1.

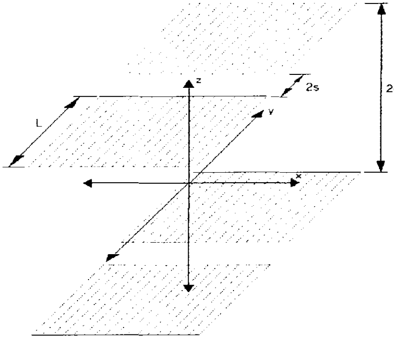

Figure 3.1 The Basic PERL Coil Layout

Design Parameters Affecting Performance Along x

Since the layout consists of identical current arrays in each of the eight octants, we will derive the field contribution of one octant and extend the relation to the other octants simply by making the appropriate sign changes, which will not be shown. As seen by an observer at any point in space, the z component of the field from octant one is derived from the Biot-Savart law as:

$$B_1 = \frac{(-1)^n I_0 \mu_0}{4\pi} \sum_{n=0}^{N} \int_{s}^{L} \frac{x + \lambda \cdot (1/4 + n/2)}{|R_1|^3} dl, \tag{3.0a}$$

where

$$R_1 = \sqrt{\left(x + \lambda \cdot \left(\frac{1}{4} + \frac{n}{2} \right) \right)^2 + (y - l)^2 + (z - d)^2}. \tag{3.0b}$$

The parameter n allows the equation to reflect the alternating direction of the current elements as well as the displacement of half the period between successive elements. The zeroth element must be displaced from the plane $x=0$ by a quarter period to generate a cosine. The parameter λ is equal to $2\pi/q_x$. Note that the parameters l and d have a parallel effect on the magnitude of the field, while λ does not since it appears in the numerator of the integral as well. Due to the complexity of the equations, much of this analysis will involve numerical or qualitative discussion of the interdependence of the layout parameters and how they manipulate the PERL field.

The distance occupied by the coils along x is obviously a function of λ and N. The number of current elements available to generate the PERL field is proportional to the inverse of λ. Assuming that all elements are of equal length and carry equal current, the field between the current sheets approaches $B \propto \cos(2\pi x/\lambda)$ as N approaches infinity. This is true since the cosine results from an infinite series of current elements, and becomes distorted if the series is truncated. Near the origin, for instance, the field resulting from $N=5$ bends upward since the current elements toward the extremities are not embedded deeply in the array. Figure 3.2, Figure 3.3, and Figure 3.4 illustrate how increasing N improves the quality of the field when all other parameters remain unchanged. The current elements are superimposed on the field plot for each of the three cases.

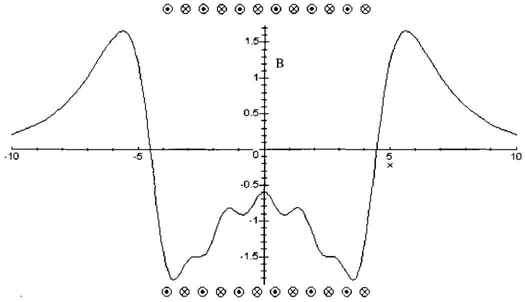

Figure 3.2 Field along x in Imaging Region for $N=5$

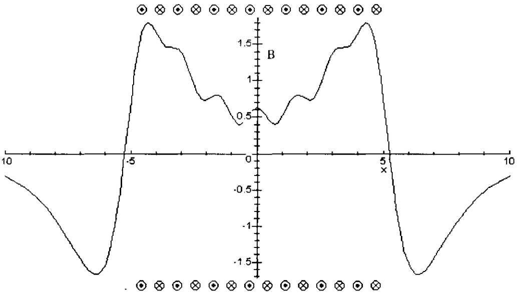

Figure 3.3 Field along x in Imaging Region for $N=6$

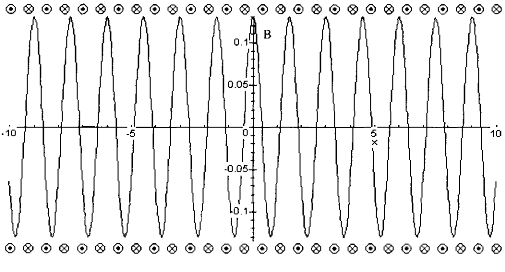

Figure 3.4 Field along x in Imaging Region for $N=100$

When N is small, the field distorts either upward or downward depending on whether N is even or odd, since the current directions alternate. The bending results from the disparity in suppression seen at different points along x. In the center, the field is highly balanced and suppressed since an equal array of current elements resides to either side. Moving toward the extremities, however, the field caused by the final element at either end of the array exerts significant influence since it has no neighboring elements on one side to dampen it. Hence, the desired cosine becomes superimposed on the field caused by the final element. If we allow the final element at either end to reside at a distance from the center such that its contribution is negligible, we seen a pure cosine waveform as in the case when $N=100$. Calculating this required distance is a trivial matter once the other parameters are known.

One strategy for reducing the bending effect along x while maintaining a constant value or N, and thus increasing the usable range along x relative to the space occupied by the coils themselves in this dimension, involves weighting one or more of the fringe elements differently so that the edge effects are minimized. This can be accomplished either by including less wire turns in the fringe elements or by adjusting the lengths to decrease the unsuppressed contribution from the fringe elements, and turns out to be convenient in other respects as well. Wrapping the PERL coils in the most efficient manner involves winding through one bank of current elements and back multiple times, meaning that the outer most elements receive only one wire wrap for every two wire wraps of the interior elements. Also, since the experimental coils fit inside a circular magnet bore, a reduction in length of the outer elements facilitated efficient use of space.

Consider the effect of the parameter L, which represents the length of the current elements. Intuitively, increasing L increases the amplitude of the PERL field at the extremities of the imaging region since the source currents occupy more space. Increasing the amplitude at the extremities causes a larger linear gradient between the peaks of the field. However, as differential current elements are added to the existing lengths, the returns of each successive addition diminish due to the increase distance from the imaging region. Indeed, for an arbitrary point in the xy plane within the imaging region, and with all other parameters held constant, the field strength as a function of L exhibits the expected characteristics as shown in Figure 3.5.

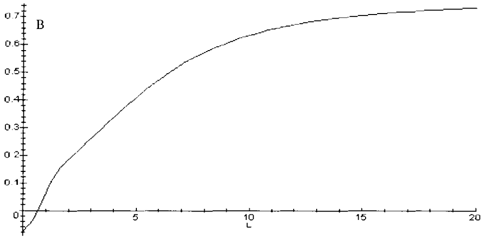

Figure 3.5 Field Strength vs. L

The distance between the current arrays along the transverse axis is given by $2 \cdot d$. As stated previously, the strength of the field increases proportionally to the inverse of the square of the distance between the current arrays. Aside from this, d plays an important role in the variation of the field with position along both x and y. For all other parameters constant and assuming N is finite, the distortion of the cosine variation along x diminishes as the distance between arrays along the transverse axis narrows. For instance, this is true near the origin since the contribution of the edge current elements increases much more slowly than the contribution from the center elements when d decreases, causing the weighted effect of the edge elements to decrease relative to the effect of the center elements. However, when d increases, the relative effect of the center elements diminishes much more rapidly than the effect due to the edge elements, until the center elements effectively nullify themselves due to their close proximity, leaving only the effect of the edge elements. Figures 3.6 and 3.7 illustrate this.

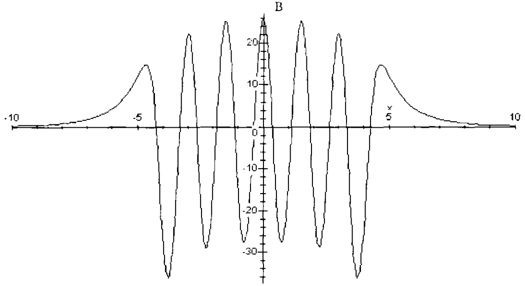

Figure 3.6 Field Pattern Along x for $N=5$ and $d / \lambda << 1$

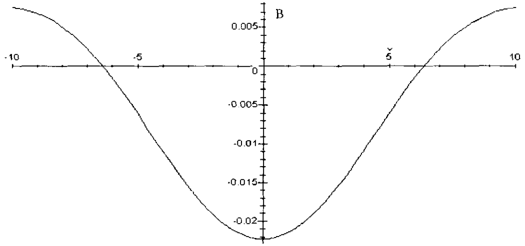

Figure 3.7 Field Pattern Along x for $N=5$ and $d / \lambda > 1$

The parameter s has, in general, an effect on the total field that is parallel in most respects to the effect of the parameter d. As mentioned previously, this is due to the appearance of both parameters in the denominator of the original equation relating field strength to position in space. Similar to the argument made for d, the elements in the center of the array will have and insignificant relative contribution to the field in the imaging region compared to the edge elements when s / λ becomes significantly larger than one, as shown in Figure 3.8.

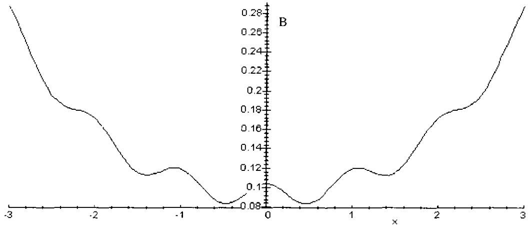

Figure 3.8 Field Pattern Along x for $N=10$ and $s / \lambda > 1$

Design Parameters Affecting Performance Along *y*

The majority of the challenge of designing PERL coils consists of compromising between the performance characteristics along the three axes, which often have opposing optimization requirements. In part this is due to the need for linearity along the y axis while maintaining periodicity along the x axis. When linearity exists over a significant region along y, it tends to extend to the performance along x, causing the deterioration of periodicity.

Consider the affect of the parameter d / λ on the field seen along y in the imaging region between the coil sets. When d / λ is less than one, the transition of the field from a positive cosine for positive y to an inverted cosine for negative y becomes concentrated, exhibiting a large gradient with good linearity in a limited region between the opposing halves of the PERL coil. The opposing halves are so named because they are inverted in phase to create the necessary transition along y. Obviously, when d / λ increases, the rate of change of the field decreases when transitioning along y in the region between the coils. We can analyze this effect by selecting a single current element from the array, since the total field is a summation of contributions that have the same form. In this case we have arbitrarily selected the zeroth element in octant 1. By making the assumption that L is infinite and s is zero to simplify the analysis, and performing the differentiation with respect to y we get:

$$\frac{\lambda\left(16\frac{y}{\sqrt{\lambda^2+16y^2+16d^2}}+4\right)uo\,Io}{\sqrt{\lambda^2+16y^2+16d^2}\,(\lambda^2+16d^2)\,\pi}-16\frac{\lambda\left(\sqrt{\lambda^2+16y^2+16d^2}+4y\right)uo\,Io\,y}{(\lambda^2+16y^2+16d^2)^{3/2}\,(\lambda^2+16d^2)\,\pi} \qquad (3.1)$$

Close examination of the expression reveals that as d / λ decreases, the gradient along y decreases, and the field has a uniform slope over a larger region. This analysis is easily extended to the field produced by an array of elements. Figure 3.9a and Figure 3.9b contrasts the case for d / λ less than one to the case when it is significantly greater than one.

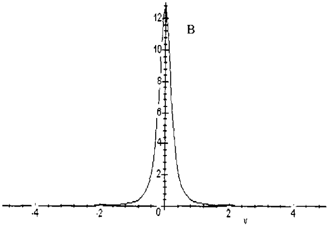

$d / \lambda << 1$

Figure 3.9a Effect of d on Gradient strength and Linear Region Along the y axis

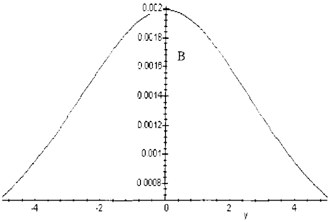

$d / \lambda > 1$

Figure 3.9b Effect of d on Gradient strength and Linear Region Along the y axis

The analysis of the performance related to s / λ follows the same steps as that for d / λ. The conceptual explanation for the effect of s / λ on the field along y is relatively simple. As s / λ increases, the field simply shifts so that there is less contribution to the imaging region, which is centered at the origin. As described previously, the periodicity along x is nullified rapidly due to the rapid falloff of the array. By again using the zeroth element of octant 1 as representative of the cumulative effect of the arrays, and making the assumption that L tends to infinity while d goes to zero to simplify expressions, we find that the derivative of the field with respect to y is:

$$\frac{\left(\frac{1}{2}\frac{32y-32s}{\sqrt{\lambda^2+16y^2-32ys+16s^2}}+4\right) uo\, lo}{\lambda\sqrt{\lambda^2+16y^2-32ys+16s^2}\,\pi} - \frac{1}{2}\,\frac{\left(\sqrt{\lambda^2+16y^2-32ys+16s^2}-4s+4y\right) uo\, lo\,(32y-32s)}{\lambda\left(\lambda^2+16y^2-32ys+16s^2\right)^{3/2}\pi} \qquad (3.2)$$

Figure 3.10 shows the derivative of the field defined by this expression for two values of s / λ.

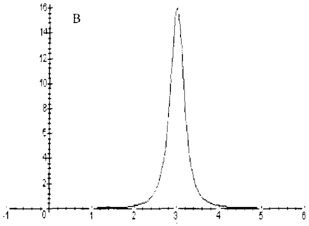

s / λ > 1

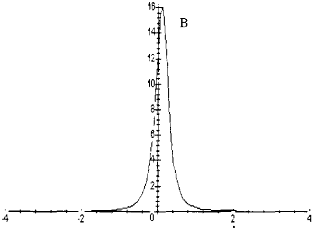

s / λ < 1

Figure 3.10 Effect of Varying s / λ on the Derivative of the Field

If we choose s / λ so that the flat region shown in Figure 5.13 extends through the imaging region, we get a low gradient strength that is relatively homogeneous. If, however, we choose s / λ so that the peak exists within the imaging region, we get high gradient strength but poor homogeneity across the imaging region.

METHODS

PERL Coil Modeling and Construction

The PERL coil configuration described previously was optimized using trial and error methods in conjunction with closed form field calculations for all primary and return current paths. A program written specifically for PERL coil field modeling performed the calculations. The coil itself was constructed by hand wrapping wire, making the target field method impractical. The computer modeling used to optimize the PERL field in a limited region also incorporated the thickness and wrapping characteristics of the wire into the model.

The final PERL coil design was selected from roughly 30 designs due to a good compromise between various aspects of the PERL field, including linearity along y and periodicity along x within the desired region, as well as gradient strength, homogeneity along z, and practicality of implementation. Figure 4.0 shows one of four identical banks of current elements and gives the final layout and parameter values for the design that was constructed.

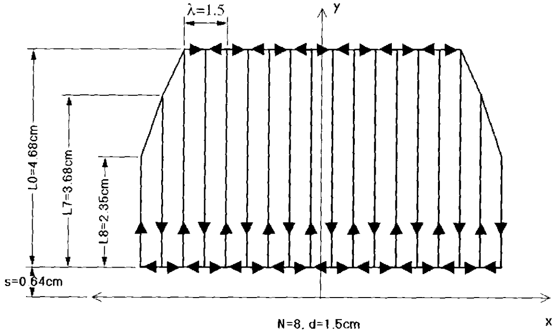

Figure 4.0 Experimental PERL Coil Design

Computer modeling was used to generate the field produced by this design, including all primary and return paths. The field in the plane $z=0$ is shown in Figure 4.1.

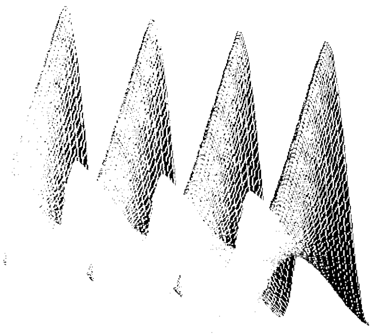

Figure 4.1 Simulated PERL Field Generated by Experimental Coil

The plot in Figure 4.1 covers a span of 6 cm on x and 2 cm on y. Outside of these boundaries the field departs from the PERL field rapidly. The field along the y axis and its derivative show significant non-linearity as compared to fields produced by conventional linear gradient coils even in the region near the origin. Figure 4.2 shows the peak-to-peak view of the field along the y axis, and Figure 4.3 shows the derivative of the field along the y axis, clearly indicating fluctuation in the slope.

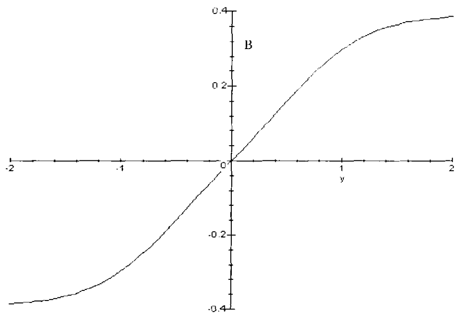

Figure 4.2 The PERL Field on the y axis

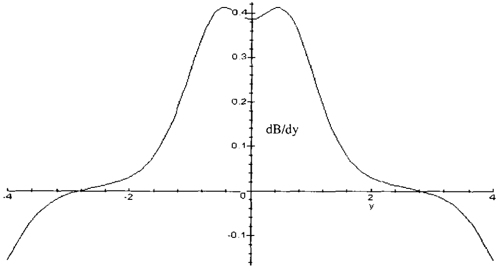

Figure 4.3 The Derivative of the PERL Field on the y axis

As Figure 4.3 indicates, the gradient strength varies from roughly 4 G/cm to 3 G/cm in the interval $y = -1..1$ cm, which represents 20% of the distance occupied by the coils in this dimension. This is a variability of approximately 25% in gradient strength within the most linear region. The periodicity of the field near the x axis is illustrated in Figure 4.4, in which a minor amount of bending in the field caused by fringe effects is apparent. The field is reasonably uniform on the interval $x = -3..3$ cm, which represents 40% of the space occupied by the coils in this dimension.

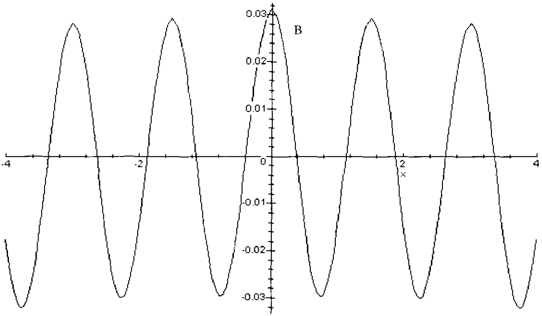

Figure 4.4 Periodicity of the PERL Field

Experimentation

Experiments were conducted by interfacing the PERL coil with the z gradient channel of a 1.5 T TecMag system. The phantom, a test tube of distilled water 1 cm in diameter, was thin enough to warrant the lack of slice selection in the pulse sequence. The primary object of the experiment was to verify the formation of an echo train under non-ideal real world circumstances. Various amount of prephasing were achieved by adjusting both the amplification and duration of the PERL coil channel to investigate the decrease in peak echo amplitude for larger amounts of prephasing. Since spacing between echoes is, in theory, inversely proportional to the strength of the readout gradient, experiments were conducted to control the echo spacing using the readout gradient strength. All experiments consisted of multiple acquisition averaging using either a non-slice selective spin echo sequence including PERL prephasing, as shown in Figure 2.0, or a non-slice selective gradient echo sequence modified to include the application of the PERL field.

Several RF coils were constructed in an effort to improve SNR after preliminary experiments proved to yield no detectable signal when conducted using RF coils that were relatively poor in quality. RF coils used to obtain results consisted of single-turn, dual Helmholtz loops designed to detect signal across the rectangular volume in the PERL field was closest to optimum. Coils were used in standard imaging sequences to verify performance prior to use in experimentation involving the PERL sequence.

RESULTS AND DISCUSSION

Most of the results do not offer convincing evidence of the formation of an echo train, however, an unusually large amount of signal remained long after the initiation of the readout gradient, suggesting increased coherence as compared to what would be expected from gradient-induced decay following the application of the readout gradient. This suggests that the PERL prephasing was causing some amount of coherence to cycle in the signal, but if so, the amount was minimal and unusable at current levels.

The echo peaks themselves could not be labeled as such with absolute certainty, however, what would presumably be the echo peaks exhibited the expected increase in inter-echo spacing in the presence of diminished readout gradient strength. For the remainder of this discussion, points in the signal that could represent the partial rephasing of spins during an echo will be termed peaks to indicate ambiguity.

One source of doubt arises from the fact that readout gradient amplitudes on the order of one-hundredth of a G/cm, which were used to in experiments in which peaks were visible and separated by 4 – 20 ms, are in fact possibly on the order of leakage offset current that flows through the coils even when no output is applied. This would seriously undermine the argument that the peak spacing was in fact affected by small changes in the readout gradient strength that may have been buried in the noise of the system.

Another possible source of ambiguity stems from normal gradient induced decay, which diminishes with readout gradient strength. This suggests that the increase in inter-peak spacing that apparently exhibited the behavior predicted by theory, might in fact have been a manifestation of decreasing gradient induced decay, since the effects of lower readout gradient strength on the PERL signal and the signal from normal gradient decay may be difficult to differentiate. If the results had been more ideal, these two potential explanations for the increase in peak spacing would not be as easily confused. For a standard gradient-induced decay, the gradient strength affects the exponential decay rate of the signal, but does not change the periodicity of the decaying signal. In a PERL experiment, however, the periodicity of the signal is inversely proportional to the readout gradient strength.

Attempts to increase the apparent cyclical coherence of the signal by using a weaker PERL field to prephase did not result in a detectable increase in peak amplitude that would indicate an increase in coherence. Since theory indicates that the PERL echo train approaches a gradient-induced decay curve as the PERL field approaches zero, the detectable coherence observed at an advanced point in time may actually diminish as the PERL field decreases. At the same time, the signal is easiest to analyze at these points in time because of the decreased effects of the FID. Therefore, while the coherence may have improved early on in the signal for weaker PERL fields, it was difficult to differentiate this from the FID.

In summary, the results can be interpreted to indicate cyclical coherence in the signal as a result of PERL prephasing, indicating potential for improvement, but did not yield a periodic signal that could conceivably be sampled to generate an image

CONCLUSIONS

Fundamentally, PERL MRI sacrifices signal coherence in order to encode the signal in a single shot without using rapidly switching gradients. This is true even if it could be implemented to yield results that agree precisely with theory. Therefore, significant SNR penalties will result with the application of stronger PERL fields since the power contained in each echo will diminish relative to the power in ambient noise.

Weakening the PERL field, however, causes the minimum resolvable distance along y to increase. The resolution in y is proportional to the product of the duration and the maximum slope of the PERL field. Non-linearity of the PERL field at a given value of x causes localized differences in slope that will lead to non-uniform resolution along y. The experimental PERL coil built for this investigation would presumably create images with a variation in resolution along y of roughly 25%.

In basic PERL MRI, resolution along x depends solely on the periodicity of the PERL coil itself, and cannot be changed by adjusting imaging parameters. The PERL coils analyzed in this investigation maintained good periodicity for only 40% of the total distance occupied by the coil in this dimension, and were extremely sensitive to the fringe elements. True periodicity along x does not occur when the effects of the fringe elements cause the periodic field to bend, and hence become non-periodic. Although there was no theoretical or experimental investigation of the effects of weighting the amplitude of the PERL field by a function of x, which occurs for bent fields, it is reasonable to believe that this would seriously alter and most likely eliminate any cyclical coherence in the signal. Due to the sensitivity of the design and the difficulty of achieving the desired precision in a hand built coil, a possible explanation for the non-ideality of the experimental results may be that the field generated by the experimental coils is not truly periodic. If experiments had been conducted with a smaller phantom, the ideality of the field may have improved, but this would have reduced the potential signal intensity as well since less spins would be available to rephase. This investigation would need to be conducted without introducing inconsistencies resulting from moving the PERL apparatus and ruining the magnet shim between experiments. This could be accomplished by placing a small test tube of water within the PERL coil and feeding a long hose into the imaging region of the PERL coil. The hose would facilitate that movement of water into and out of the PERL field. Such an experiment could also experimentally verify the formation of lobes in the PERL echo resulting from the higher frequency spins present in the hose, which would occupy more space along x. Future work should seek to investigate the effects of non-idealities in the PERL field on the formation of echoes by performing computer simulations and examining the field created by the experimental coil built for this investigation. This could be accomplished by turning on the PERL field prior to the sampling of k-space using the conventional spin echo sequence, resulting in an image with different T2* weighting for different spins within the sample. Another image could be made without the PERL-imposed T2* effects, and the difference between the two images could then be taken to create a map of the PERL field.

An unusual aspect of PERL MRI stems from the changes in the signal resulting from the positioning of the phantom in the field. Unlike linear gradients, both the size and position of the phantom can significantly alter the signal due to the localized variability of the PERL field. Additional experiments should also employ methods similar to those already described to investigate the changes in the signal resulting from changing the placement and orientation of the phantom relative to the PERL field.

Although PERL MRI undoubtedly suffers from SNR penalties due to lowered coherence, it may be a potentially important form of MRI in certain circumstances that have not yet been identified. While PERL is mathematically elegant, the design and construction of PERL coils that provide performance comparable to current linear gradient coils with respect to coil size, usable imaging region, and gradient strength represents a significant engineering challenge.

REFERENCES

[1] S. Patz, M.J. Hrovat, Y.M. Pulyer, and F.J. Rybicki, "Reconstruction algorithm for novel ultrafast MRI," *Int J Imaging Syst Technol* , vol. 10, pp. 216-224, 1999.

[2] F.J. Rybicki, S. Patz, M.I. Hrovat, and Y.M. Pulyer, "Reconstruction algorithm for novel ultrafast MRI," *Int J Imaging Syst Technol* , vol. 10, pp. 209-215, 1999.

[3] S.M. Wright, "NMR-MRI," Chapter 16 in *Introduction to Biomedical Engineering*, John Enderle, Susan Blanchard, Joseph Bonzino, Eds., Academic Press, NY, 1999.

[4] P.M. Jakob, M. A. Griswold, K.O. Lovblad, Q. Chen, R. R. Edelman, "Half-fourier BURST imaging on a clinical scanner," *Magn. Reson. Med.*, vol 38, pp. 534-540, 1997.

APPENDIX A

FUNDAMENTALS OF MRI

Magnetic resonance imaging is a process that measures the free induction decay of quantum nuclear spin states in the presence of magnetic field gradients and shaped RF pulses, and decodes the information into image data. Basic MRI analysis consists of spatially encoding a slice of the specimen and mathematically constructing an image from the selectively sampled decay rates of the magnetic dipoles of its constituent nuclei. All MRI technology has these fundamental attributes in common, making them central to the PERL experiment discussed in this paper.

Although an understanding of MRI techniques is possible without consideration of quantum mechanics, the behavior of the nuclei cannot be appreciated and the extent of the MRI concept not fully realized without addressing spin states. Two quantum numbers, I and m, characterize the spin states of the nuclei. If I is integral or half-integral, the nuclei can be exploited in MRI analysis due to its magnetic properties. Fortunately, the hydrogen proton, which exists in most organic matter, exhibits this trait. The relation

$$m = \pm I, \pm(I-1), \ldots, 0$$

gives the number of distinct energy states [3]. The energy difference between the states of a spin ½ nucleus like the hydrogen atom is given by

$$\Delta E = (E_{-1/2} - E_{1/2}) = \gamma\hbar B_0$$

where $\hbar$ is Planck's constant divided by $2 \cdot \pi$, γ is the nuclei specific Larmor ratio, and B_0 is the static magnetic field, usually z-directed [3]. The local static magnetic field, then, determines precisely what frequency an incident photon must have to induce a transition between energy levels, and this principle is exploited in selecting specific nuclei by manipulation of the ambient static magnetic field.

Each quantum spin state carries a magnetic dipole moment with z component given by the equation [3]:

$$\mu = \gamma\hbar m.$$

We can visualize the z component exclusively since we will be dealing with a large number of spin vectors forming a net magnetic dipole moment in the positive z direction, which is slightly preferred as the low energy position in the presence of a positive z-directed B_0 field. We can then consider the summation as an isolated spin and apply classical mechanics along with the relationship between spin frequency and the static magnetic field to obtain the Bloch equation [3]:

$$\frac{d\vec{\mu}}{dt} = -\gamma\vec{B}_0 \times \vec{\mu}.$$

The equation correctly asserts that the magnetic dipole moment vector aligns with the z axis in the equilibrium position for the z-directed static magnetic field. However, should an x or y directed RF pulse of the proper frequency be applied, the dipole moment will begin both to tip from the z axis as well as to precess about it. The exact behavior depends upon the time variation of the applied magnetic field, B_1, and conforms to the equation [3]:

$$\frac{d\vec{M}}{dt} = -\gamma\vec{M} \times (\vec{B}_0 + \vec{B}_1)$$

where M represents the summation of all individual magnetization vectors. The displacement of the magnetization vector in the presence of the applied photons will induce a resultant time-varying field that can be detected on a properly designed receiving coil. This forms the basis for MRI stimulus and feedback.

As previously stated, the displaced magnetization vector will precess, and therefore lends itself to study within a rotational frame as opposed to the laboratory frame. The rotational field will have the same frequency of oscillation as the magnetization vector, thereby forcing the B_0 field to be zero within the rotational frame and leaving the B_1 field, chosen to be essentially constant in the rotating frame, to solely induce the torque on the magnetization vector within the rotational frame. This torque, in conjunction with the magnetization vector, is responsible for precession of the magnetization about the B_1 vector and the subsequent tip angle. In the laboratory frame the magnetization vector will precess about two axes for the duration of the B_1 pulse, and will precess about the z axis only until its energy has been dissipated.

The tip angle, measured from the z axis, is proportional to the product of the magnitude and duration of the rotational B_1 field by γ. The two most important cases in basic MRI are the $\pi/2$ and π pulses, named for the extent to which they tip the magnetization from the z axis.

Energy dissipation occurs due to relaxation processes until the net magnetization vector has returned to equilibrium along the z axis. The two relaxation processes that effect this return are characterized by either a longitudinal or transverse loss of energy. The T_1 process is an exponential process characterized by a loss of energy to the surrounding lattice in which the magnitude of each magnetization vector diminishes. The T_2 process is also an exponential process characterized by the dephasing of the components of the aggregate magnetization vector resulting in a progressively smaller signal. Dephasing is caused by the variations in rotational frequency due to inhomogeneities introduced by interactions with neighboring atoms with associated T_2 time constant, non-ideal B_0 fields with associated T_2^* time constant, and magnetic field gradients with associated T_2^{**} time constant. Since T_2 varies with nuclear environment, we desire techniques to isolate it from the effects of the MRI equipment, given by the T_2^* and T_2^{**} time constants. The T_2^* time constant is related to T_2 by

$$\frac{1}{T_2^*} = \frac{1}{T_2} + \frac{\gamma \Delta B_0}{2}$$

where ΔB_0 is the range of the magnetic field occupied by excited spins [3]. The T_2^{**} time constant reflects these affects as well as gradient-induced decay, given by

$$\frac{1}{T_2^{**}} = \frac{1}{T_2} + \frac{\gamma \Delta B_0}{2} + \gamma G r$$

where G is the gradient strength and r is the object radius [3].

Creation of a gradient echo, the most basic approach to nullifying the effects of a gradient along x in the total magnetic field, relies on reversing the dephasing along the x axis prior to data collection. This subsequently reverses the precessions of the dipoles in the xy plane, and causes frequency to vary linearly along the x axis. When a gradient along x is applied in the opposite direction, it gradually rephases the magnetization along the x axis, reaching a peak when the variation of both frequency and phase is zero along the x axis.

The second popular approach, termed spin-echo, causes an echo to form that carries primarily T_2 information. In principle, if the spins rotate 180° about either the x or y axis while undergoing normal precession, they will rephase with an aggregate magnitude that is independent of the spatial magnetic field variations. If TE is the amount of time from the initial tipping of the dipoles into the xy plane occurring at the time origin to the formation of an echo, then $TE/2$ designates when the 180° flip occurred. This can be visualized by analogy to runners on a track. If the runners begin running at different constant speeds at the time origin and change direction after a time $TE/2$, then they will return to their starting position at exactly time TE.

The sequence of steps taken to collect image data from the sample begins with slice selection, which is the part of the object that will be seen in the two-dimensional image. As previously shown, the local Larmor frequency of oscillation of the sample nuclei is directly related to the applied B_0 field by the nuclei specific Larmor ratio. If a z-directed gradient magnetic field is applied such that the total field is given by

$$\vec{B}(\vec{r}) = (B_0 + \vec{G} \cdot \vec{r})\hat{a}_z$$

where G is the gradient strength, there is a link between position along the z axis and Larmor frequency that is easily exploitable in exciting a specific slice orthogonal to the z axis. Recall that an x or y-directed magnetic field varying as a sinusoid at the Larmor frequency of a given nucleus is approximated in the rotational frame as a constant field. By making the "small tip-angle" approximation, which states that the for small tip angles, the tip angle is linearly related to the RF pulse power [3]:

$$M_{XY}(z) = 2\pi M_Z^0 e^{-j\gamma G_z z T/2} F^{-1}\{B_1(t)\}.$$

Therefore, a slice of nuclei can be excited by applying an x or y directed B_1 field in the form of a sinc function of the appropriate amplitude, bandwidth, and center frequency. As soon as the z-directed dipoles begin to tip toward the xy plane, their z-related Larmor frequencies will cause them to dephase along the z axis, as evidenced by the complex exponential factor in the previous equation. This position-dependent phase shift can be "rewound" by applying a gradient pulse of opposite sign for the same length of time as the slice selection pulse. The phases will then realign, and there will be no spatial frequency variation upon the completion of the rewind pulse.

Once the slice has been chosen, we require a technique to spatially encode the field induce decay into the received signal so that nucleus-specific relaxation times can ultimately be mapped to the xy plane, generating an image. A popular technique to do this relies on orthogonal gradients to link Larmor frequency to position along the x axis, and phase to position along the y axis. The signals are generated and discretely sampled repeatedly until enough data has been collected to take a two-dimensional inverse Fourier transform and reconstruct the image.

The received signal will not be a function of position without the application of gradients, since Larmor frequency will be constant throughout the slice. First we must develop the signal in the absence of gradients by incorporation of the relaxation effects into the Bloch equation to yield the modified Bloch equation [3]:

$$\frac{d\vec{M}}{dt} = -\gamma\vec{M} \times \vec{B} - \frac{M_X \hat{a}_X + M_Y \hat{a}_Y}{T_2} - \frac{(M_Z - M_Z^0)\hat{a}_Z}{T_1}$$

with a transverse magnetization solution and equivalent forms [3]:

$$\vec{M}_{XY}(t) = M_{XY}^0 (\hat{a}_X \cos\omega_0 t - \hat{a}_Y \sin\omega_0 t)e^{-t/T_2},$$

$$\vec{M}_{XY}(t) = M_{XY}^0 e^{-t/T_2} \operatorname{Re}\left\{(\hat{a}_X - j\hat{a}_Y)e^{-j\omega_0 t}\right\}$$

Manipulation of Maxwell's equations gives the relation for the voltage in a coil with sensitivity [3]:

$$B_{1r} = \frac{\vec{B}_1}{I_1} \cdot \frac{(\hat{a}_X - j\hat{a}_Y)}{\sqrt{2}}.$$

The voltage induced in the coil is then [3]:

$$v(t) = j\sqrt{2}\omega_0 \Delta V M_{XY}^0 B_{1r} e^{-t/T_2} e^{-j\omega_0 t}.$$

The preceding equations outline the derivation of the fundamental relationship between the properties of a unique localized volume element of the nuclear environment and the resulting voltage signal occurring in a detector coil, which will ultimately be used to sample the aggregate time-varying signal to collect data for image reconstruction.

The application of gradients allows the received signal to carry with it information about the composition of the signal relative to points in the sample slice. Through the technique of frequency encoding, this can be accomplished along the x axis. An z-directed gradient along x is added, and the volume integral represents the total signal over the volume of the slice, giving [3]:

$$S(t) = \iint_{slice} j\frac{1}{\sqrt{2}}\omega_0 \Delta z M_{XY}^{0} B_{1t} e^{-t/T_2} e^{-j(\omega(x)-\omega_{mix})t} dxdy.$$

Since we consider the slice to be thin, we can assume homogeneity in z. The parameters of interest here are M_{XY}, B_{1t}, and T_2 because they are spatially dependent. The image at a point is:

$$I(x,y) = j\frac{1}{\sqrt{2}}\omega_0 \Delta z M_{XY}^{0}(x,y,z) B_{1t}(x,y,z) e^{-t/T_2}.$$

So an expression for the received signal at the coil is [3]:

$$S(t) = \iint_{slice} I(x,y) e^{-j(\omega(x)-\omega_{mix})t} dxdy.$$

The x-dependent component of the angular frequency is expanded as [3]:

$$\omega(x) = \omega_0 + \gamma G_x x.$$

Now, if the signal is passed through a quadrature demodulator and mixed with a signal equal in frequency to the B_0 induced frequency, we can eliminate the ω_0 component in the exponent and write [3]:

$$S(t) = \iint_{slice} I(x,y) e^{-jk_x x} dxdy.$$

Here k_x has replaced $\gamma G_x t$. This means that the received signal is the Fourier transform of the projection of the image on the x axis. To obtain the whole two-dimensional image it is necessary to encode along the y axis as well. Obviously k_x represents both the Fourier domain variable and a spatial phase change that increases both linearly along x and linearly with the amount of time the gradient has been applied. In other words, the longer the frequency variation along the x axis lasts, the more phase difference will accumulate. Therefore, sampling of the signal value as time increases is the same as sampling along the k_x axis. The time origin coincides with the k_x origin, creating a complication with the inverse transformation process. This will be addressed shortly.

Generation of a two-dimensional image requires knowledge of what is called k-space, which is the two-dimensional spatial frequency composition of the signal. Each point in the image map depends on the accuracy of knowledge of the entirety of k-space. As has been shown, if we only know one line of k-space, then only a single line representing the summation of all image data along the orthogonal axis can be generated. A technique known as phase encoding allows us to shift away from the origin of k-space along the y axis.

Similar to the concept of frequency encoding is the concept of phase encoding. While the two encoding techniques stem from the concept of gradients, the difference arises due to the sampling of the signal during the frequency-encoding pulse, causing the rate of phase change along x to increase with time. The phase encoding pulse has a magnitude G_p and duration T_p during which data is not collected. Since this step precedes the frequency-encoding step, the effect seen along the y axis during data collection exhibits no frequency variation, hence the name phase encoding. Thus, the signal can now be represented as the two-dimensional Fourier transform [3]:

$$S(t) = \iint_{slice} I(x, y) e^{-jk_x x} e^{-jk_y y} \, dx dy.$$

Phase and frequency encoding pulse sequences can facilitate the full sampling of k-space. Partial saturation is the most basic sequence. First, the slice selection gradient and RF pulse are applied simultaneously, followed by phase rewind pulse that creates a gradient along z. The phase encoding magnitude, arising from the gradient along y, is unique to each sequence, while the duration remains unchanged. For each repetition, the sampling occurring during the frequency-encoding step will occupy a unique line of k-space. Finally, a gradient along x is applied and the read coil performs sampling. This sequence of steps is repeated for all desired values of k_y, and then the data is inverse Fourier transformed and interpreted to generate the image.

In the preceding discussion, the center of k-space along the x-axis is measured at the beginning of each frequency-encoding gradient. This means that the left half plane of k-space cannot be sampled. While there are techniques to overcome this without more sampling, fundamentally we wish to be able to sample all of k-space. A gradient-echo sequence is the simplest way to accomplish this.

During each repetition of the gradient-echo sequence, the addition of a frequency-encoding gradient applied at the same time and for the same duration as the phase encoding gradient causes the ensuing sampling to begin at a point along the negative k_x axis. This point depends on the applied gradient strength. The initial frequency-encoding gradient is applied in the opposite direction as the primary frequency-encoding gradient, inverting the rate of phase change seen along x. Both of gradient applications occur within the same cycle. Thus, the spins will be dephased to a chosen point on the k_x axis by the beginning of sampling, and the gradient applied during the sampling will rephase them, achieving a peak at time t2 measured from the start of sampling [3]:

$$G_{x,1} \cdot T_{x,1} = G_{x,2} \cdot t_2 .$$

Beyond time t2 the coil samples points along the positive k_x axis because the spins have begun to dephase in the positive direction.

There are two major problems with the pulse sequence just described. Recall that net magnetization vector in the xy plane will begin to undergo relaxation processes due to a number of factors. Therefore the magnetization detected in the coil will have already undergone a good deal of relaxation before the signal can be sampled, and that means that less samples can be taken before the signal has diminished to an unusable state. Also, the sampled signal will reflect decay caused by magnetic field inhomogeneity, undermining the detection of the natural decay caused by the nuclear environment that characterizes the atomic makeup of the sample.

The most ingenious method to eliminating losses due to magnetic field inhomogeneity relies on the spin-echo technique discussed previously. Recall that if all of the spins in the xy plane are initially aligned right after being tipped, the magnetic field inhomogeneity will induce magnetic field variation in the data collection process will result in position dependent phase shifts throughout the sample after some amount of time, $TE/2$, measured from the initial tipping. If, at $TE/2$, all of the rotations are flipped 180° about the x or y axis, the signal will nullify dephasing due to experimental field variations at time TE, and carry with it only spatially encoded information on naturally induced decay.

The spin echo sequence is analogous to the gradient echo sequence, but the initial frequency-encoding gradient, occurring prior to the 180° flip, will have the same direction as the next frequency-encoding gradient, occurring after the 180° flip. Because the spins have been flipped, a gradient along x of the same sign causes them to realign at TE. The flipping procedure is analogous to slice selection, but the phase variation along the z axis is rewound by the conjugation of k-space by the flipping pulse, and the power contained in the RF pulse is greater in order to achieve greater flip angle.

Resolution and Field of View

Data collection through the sampling of k-space must occur at discrete intervals. Since sampling requires time, there is a limit to the amount of sampling that can occur before the signal decays below noise levels. Both the extent of the k-space plane that is sampled and the rate at which it is sampled determine the resolution and field of view of the image. The relationship between sampling resolution and field of view along the x and y axes is [3]:

$$FOV_X = \frac{2\pi}{\Delta k_x}, \quad FOV_Y = \frac{2\pi}{\Delta k_y}$$

Since sampling occurs at time intervals under a constant frequency-encoding gradient, the resolution in k_x is related to the time between samples by [3]:

$$\Delta k_x = \gamma G_x \Delta t.$$

Combining this equation with the previous equation, and defining field of view in x as $N\Delta x$, the resolution along the x axis of the image is [3]:

$$\Delta x = \frac{2\pi}{N\gamma G_x \Delta t}.$$

The preceding relationships apply to the phase encoded y axis as well, but the k_y axis is traversed by incrementing the phase encoding gradient strength as opposed to its duration. This preserves constant repetition time. Therefore, the relationship for resolution along the y axis is [3]:

$$\Delta y = \frac{2\pi}{N\gamma G_y T_p}.$$

Contrast

By designing pulse sequences that manipulate the weighting of image parameters, we can accentuate details of specific injury processes or diseases. In particular, images generated using pulse sequences designed to give T_1 weighting will provide different information than those weighted by T_2. Typically, appropriate values of TE and TR can optimize contrast between two different types of tissue.

Consider both the transverse magnetization, M_{XY}, and the longitudinal magnetization, M_Z, for the partial saturation sequence. At time t = 0, prior to application of the slice selection pulse, we have:

$$M_{XY}(0) = 0 \text{ and } M_Z(0) = M_Z^0 \ .$$

The RF pulse tips the spins into the xy plane, during which time the T_1 and T_2 relaxation effects are insubstantial. Following the RF pulse the magnetization components are:

$$M_{XY}(0^+) = M_Z^0 \ ,$$

$$M_Z(0^+) = 0.$$

The magnetization components immediately preceding the second RF pulse are:

$$M_{XY}(TR) = M_Z^0 \ e^{-TR/T1} e^{-TR/T2} \ ,$$

$$M_Z(TR) = M_Z^0 \ (1 - e^{-TR/T1} \ ).$$

Since T_1 characterizes the rate of longitudinal return to the equilibrium position, M_Z has been partially restored. After the second RF pulse has rotated the partially restored longitudinal magnetization back into the transverse plane, we have:

$$M_{XY}(TR^+) = M_Z^0\ (1 - e^{-TR/T1}) + M_Z^0\ e^{-TR/T1} e^{-TR/T2}\ ,$$

$$M_Z(TR^+) = 0.$$

The transverse magnetization now consists of both the original transverse components and the contribution of the longitudinal magnetization from the second RF pulse. At the end of the cycle, we have:

$$M_{XY}(2TR) = [M_Z^0\ (1 - e^{TR/T1}) + M_Z^0\ e^{-TR/T1} e^{-TR/T2}]\ e^{TR/T1} e^{-TR/T2}\ ,$$

$$M_Z(2TR) = [M_Z^0\ (1 - e^{-TR/T1}) + M_Z^0\ e^{-TR/T1}]\ (1 - e^{-TR/T1}),$$

$$= M_Z^0\ (1 - e^{-TR/T1}).$$

The transverse magnetization consists of the product of the transverse magnetization at the beginning of this cycle and the decay factors. The longitudinal field that has returned clearly simplifies to the longitudinal field at the end of the last cycle, indicating that the process has reached equilibrium. Upon rotation into the transverse plane at the beginning of the N^{th} cycle, the transverse magnetization is dominated by the T_1 weighted term:

$$M_{XY}(N \cdot TR^+) \approx M_Z^0\ (1 - e^{-TR/T1}).$$

Therefore the partial saturation sequence is useful for generating T_1 weighted images. Similar derivations illustrate how other sequences can be exploited to produce T_1, T_2, or spin density weighted images. Consider the spin-echo sequence with transverse magnetization given by:

$$M_{XY}(x, y) = M_Z^0(x, y)\ (1 - e^{-TR/T1(x,y)})\ e^{-TE/T2(x,y)}\ .$$

By manipulating the TR and TE times of the pulse sequence relative to the T_1 and T_2 times of the sample, the image can be weighted according to the goals of the experiment. For instance, a T_1 weighted image can be obtained by setting TE to be short relative to T_2, and allowing TR to be on the same order as T_1. Alternatively, the use of a long TR will eliminate the T_1 term, leaving T_2 to determine contrast. Lastly, making TR very long and TE very short will result in an image weighted by the spin distribution, $M_Z^0(x, y)$.

Radio-frequency Coils

Radio-frequency coils in MRI serve two purposes. Energy flows into the sample in the form of the B_1 field from the RF coil, encoding exciting the magnetization into higher energy quantum states during slice selection and flipping processes. RF coils detect echoes from the sample and convert the field energy into an electron flow that can be filtered and analyzed during image reconstruction. However, this flow of electricity in the coil itself generates a voltage associated with thermal noise effects. In order to design coils that are as insensitive to noise voltage as possible, engineers rely on the derived signal to noise ratio for coils. To begin with, signal voltage in the coil for a MRI process demonstrates the following relationship [3]:

$$|V_{sig}| = \sqrt{2}\omega_0 \Delta V M_{XY} |B_{1t}|$$

where ω_0 is the Larmor frequency, ΔV is the volume, M_{XY} is the equilibrium transverse magnetization., and B_{1t} is the effective RF flux density. If the coil has resistance, R_{coil}, the noise voltage obeys the relationship [3]:

$$V_{noise} = \sqrt{4kT\Delta f R_{coil}}$$

where k is Boltzmann's constant, T is temperature in Kelvin, and Δf is the bandwidth of the signal. By taking the ratio of signal to noise and eliminating the constants that remain unchanged from voxel to voxel, the signal to noise ratio, or SNR, becomes [3]:

$$SNR_C = \frac{\sqrt{2}|B_{1t}|}{\sqrt{R_{coil}}}.$$

This simplified form is more meaningful for the purposes of coil design, because its terms are determined solely by the flux density and noise the coil produces while transmitting. If the SNR given by this relation is good, it will in general also perform well during MRI processes in which the actual SNR is more precisely defined and varies with position.

The greatest difficulty in determining the transmission SNR of a given coil arises due to the complexity of defining the magnetic flux density, B_{1t}. While complex modeling techniques exist that give an accurate prediction of the flux density, the Biot-Savart law often provides the most practical approach. As a reminder, the Biot-Savart law is [3]:

$$\vec{B}(\vec{r}) = \frac{\mu}{4\pi}\int_l \frac{I(\vec{r}\,')d\vec{l} \times \hat{a}_R}{R^2}.$$

This relationship defines the flux density in terms of attainable parameters for a known current distribution, and can be evaluated with numerical methods. Fortunately, since most coils fall into one of three categories in MRI, the flux densities have been well defined. These categories are circular, solenoid, and birdcage coils.

Gradient Coils

As previously stated, the application of z-directed gradients during the MRI process establishes the critical link between space and frequency. Ideally the gradient coils only create a linear variation in field strength solely along one axis, however, depending on the configuration, some fluctuation occurs along the transverse axes as well. Again, the Biot-Savart law is applicable.

Consider a basic pair of circular loop coils aligned to face each other, one at z = A, and the other at z = -A. This is a common configuration for effecting a gradient along the z axis. If equal currents flow counter-clockwise in one coil and clockwise in the other, the Biot-Savart law asserts that the net B_1 magnetic field in the plane given by z = 0 will be zero, because the contributions from each coil are equal and opposite.

In general, the z-directed variation along the z axis is an odd linear function and conforms to $B_1(z) = -B_1(-z)$.

The Biot-Savart law is also useful in analyzing saddle coils, which can be used to create z-directed gradients along the x and y axes. Because saddle coils are geometrically more complex than circular coils, with currents that must be considered in transverse planes, the precise description of their characteristic fields will not be described here.

APPENDIX B

BURST IMAGING

In introducing traditional MRI sequences and illustrating the mathematical principles that encode spatially variation into the signal from a stimulated sample, we have demonstrated the functionality of MRI without regard to image acquisition time. Traditional techniques are capable of generating high resolution images, but the time required to do so prohibits their use in dynamic imaging applications. Many candidates for MRI analysis, such as the heart, brain, and nervous system, introduce time limitations for acquiring useful data. Devising high resolution, ultra-fast imaging sequences is the goal of today's MRI researchers, yet opportunities remain to engineer low cost, ultra-fast, versatile MRI systems.

BURST imaging represents a relatively unique ultra-fast MRI process in that it acquires data in a single-shot excitation sequence without employing high frequency gradients, as is required in echo-planar imaging, among others. For BURST imaging, the acquisition of image data occurs on a time scale of roughly 10-100ms, while an echo-planar sequence typically requires 25-150ms [4]. The elimination of high frequency gradients, however, motivates BURST research. The advantages of drastically reducing gradient-switching steps stem from the stringent design requirements, high power consumption, and high cost of ultra-fast imaging systems in which high frequency gradients allow the traversal of k-space in a single-shot. With regard to gradient slew rates, for instance, the relatively lax requirements of BURST sequences allow them to be implemented on virtually any MRI system. BURST is relatively impervious to magnetic field inhomogeneity and requires minimal RF power deposition. In addition to simplifying the necessary equipment, BURST and related techniques eliminate the possibility of undesirable neurological effects induced by high-frequency gradients.

Unfortunately, the benefits of BURST techniques come with heavy penalties, which are responsible for its current lack of representation among systems in clinical use. As we will see, the inherent low SNR of BURST methods severely limits the maximum obtainable resolution.

Unlike the spin echo and gradient echo sequences described previously, which acquire one line of k-space per repetition, BURST sequences rely on the formation of an echo train that contains all of the necessary k-space data to reconstruct an image in a single repetition. Consider the following simple BURST sequence, shown in Figure B-0. There are five RF excitation pulses to generate five echoes, and each echo will be sampled five times.

First, a constant amplitude frequency-encode gradient is applied simultaneously with N low power RF pulses occurring at an inter-pulse spacing of length T. This process is known as BURST excitation. Following the final RF pulse is a 180° flipping pulse with a bandwidth chosen in conjunction with a slice selection gradient to excite only a slice of the sample. Now the phase-encoding gradient is applied under the principle of the gradient echo sequence, in which the spins along the y axis are moved to the negative extremity of the k_y axis upon initialization of the read, or frequency-encoding, gradient. Finally, the frequency-encoding gradient is applied with the same amplitude as before, while the phase-encoding gradient is applied with an amplitude that will yield sampling of the origin of k-space halfway through the application of the read-gradient.

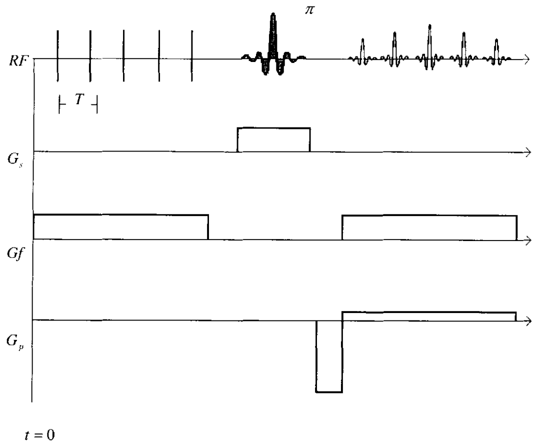

Figure B-0 A Basic BURST Sequence to Generate a 5×5 Tomogram.

Noting that the time center of this sequence occurs during the flipping RF pulse, and realizing the effect of the previously discussed spin-echo sequence, we conclude that the resulting train of echoes mirrors the BURST excitation RF pulses. Since the entire sample was initially excited, but only the selected slice experienced the frequency-encode gradient necessary to rephase its magnetization, the remainder of the transverse magnetization in the sample will have dephased to the point that it will contribute virtually nothing to the signal detected in the read coil.

To visualize the BURST process, consider two nuclei—one at the origin of the volume, labeled *nucleus 1*, and one on the x axis at the edge of the sample, labeled *nucleus 2*. Thus, the gradient along x will have no effect on the Larmor frequency of *nucleus 1*, but will contribute a maximum field and maximum change in Larmor frequency to *nucleus 2*. For simplicity, this process will yield a 2×2 pixel tomogram, meaning that only two BURST excitation pulses are required. The first RF pulse, labeled *pulse 1*, occurs at the time origin and causes the z-directed magnetization to tip by a small angle into the transverse plane. Immediately after the tipping pulse, the nuclei while have transverse magnetization vectors, as shown in Figure B-1 and Figure B-2:

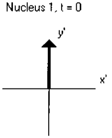

Figure B-1

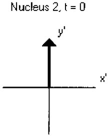

Figure B-2

After the frequency-encoding gradient of strength G_f has lasted for time T, *nucleus 1* will have a transverse magnetization component at an angle of $90°$ measured from the positive x' axis in the rotating frame, while the transverse magnetization of *nucleus 2* will have acquired angle $90° + \theta$. For simplicity we will ignore the effects of T_2 relaxation, and attribute the phase entirely to the gradient. *Pulse 2* also occurs at time T , causing the T_1 decay-induced magnetization along the z axis to tip by a small angle toward the transverse plane. The frequency-encoding gradient switches off at time T^- , at which the transverse magnetization of *nucleus 1* will still have an angle of 90° in the rotating frame, and the transverse magnetization of *nucleus 2* will consist of a transverse magnetization component at an angle of 90°+θ , as well as a transverse magnetization component at an angle of 90°, as shown in Figure B-3 and Figure B-4:

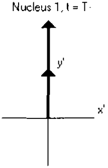

Figure B-3

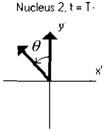

Figure B-4

The application of the slice selection gradient and the 180° RF pulse now occur at the midpoint of the sequence, enveloping the nuclei of interest in the slice. As a result of the flip about the x' axis, *nucleus 2* will have a transverse magnetization component along the negative y' axis and a transverse magnetization component at 270° - θ in the transverse plane, while *nucleus 1* will only have a transverse magnetization component at 270° in the transverse plane. Since the nuclei lie on the x axis, we will disregard the phase-encoding gradient in this description. As soon as the read gradient turns on, again with magnitude G_f, the peak of the Hahn spin echo occurs as a result of contributions from both nuclei, and begins to dephase in the presence of the gradient. This echo, denoted *echo 2*, formed as a result of *pulse 2* and is manifested by the contribution of magnetization vectors aligned with the negative y' axis from both nuclei, as shown in Figure B-5 and Figure B-6:

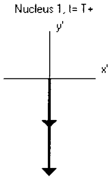

Figure B-5

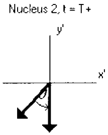

Figure B-6

After an amount of time $2T$ has passed, the magnetization component of *nucleus 2*, originally at 270° - θ, will again increase in phase by θ to align with the magnetization of *nucleus 1* and form an echo. This echo, denoted *echo 1*, occurred as a result of *pulse 1*, as shown in Figure B-7 and Figure B-8:

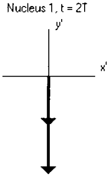

Figure B-7

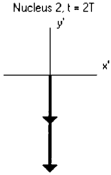

Figure B-8

The magnitudes of the magnetization vectors here do not represent any relaxation for the sake of simplicity. Although this description represents a vast simplification, it illustrates the formation of an echo train that mirrors the BURST excitation pulses.

In order complete the explanation of events with the BURST sequence, we must consider the effects of T_2 relaxation, which is responsible for the differentiation between the constituent nuclei in the image. Since T_2 relaxation cannot be reversed and progresses with time, *echo 1* will lose more power to T_2 and T_1 relaxation than will *echo 2*. Each successive echo will be diminished by a factor of e^{-2T/T_2} from the last, where T is the inter-echo spacing. Referring to the previous example, it is clear that the transverse magnetization resulting from *pulse 1* experiences relaxation effects for an amount of time $2T$ before *echo 1* forms. Again, this is due to the time symmetry between RF pulse excitation and echoes. Evidently, then, long data acquisition times result in weaker echoes at the end of the train, in turn reducing the SNR and thus limiting the image resolution.

Also missing from the sequence description are details on sampling and the traversal of k-space. Recall that the sequence employs a gradient echo scheme along the phase-encode axis to move the initial sampling to the extremity of quadrant three in k-space. Noting that the phase-encode gradient is constant during sampling, we conclude that the lines of k-space will have some amount of skew. If, however, the *y* gradient is pulsed instead of remaining constant, k-space will be fully orthogonal. As increases toward the origin, the echoes rephase along the *y* axis, reach a maximum value at the origin of k-space and then begin to dephase in the opposite direction. The alignment of magnetization along the *y* axis occurs halfway through the read-gradient. The read-coil samples each echo N times, forming a single skewed line of k-space. The N echoes occur at N distinct average values of k_y, yielding the $N \times N$ tomogram depicted in Figure B-9.

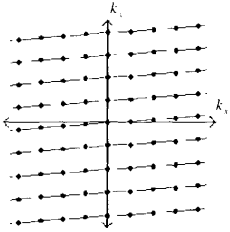

Figure B-9 Skewed K-space Sampling

Limitations of BURST

As mentioned previously, the SNR for a BURST sequence severely limits contrast and field-of-view, rendering it inadequate for a great many applications. The BURST excitation method gives rise to a different diffusion attenuation and T_2 decay for each echo, yielding a spectrum of variation that broadens with increased number of excitation pulses. The number of excitation pulses, however, determine the resolution and range of k-space sampling, meaning that the desired image FOV and resolution are in many cases not achievable. In addition, the signal decay between echoes causes a high degree of imbalance between the upper and lower halves of k-space, which causes image artifacts such as blurring to occur.

The SNR for a BURST experiment with constant spin density, D, and uniform T_2 and T_1 throughout the sample can be derived as follows. Using a simple projection scheme in which the image data is projected onto the x axis, the image is given by the discrete Fourier transform [4]:

$$I(x) = \Delta k_x \sum_{i=-(N/2)}^{(N/2)-1} \alpha(N,T_2,D) \cdot \beta(N) \cdot S(i\Delta k_x) \cdot e^{j2\pi i\Delta k_x x}.$$

The two factors, α and β, reflect attenuation of the signal due to echo number, N, as well as the sample specific properties, D and T_2. The damping factor α can be derived from the Stejskal and Tanner formula provided for a bipolar gradient-pulse diffusion experiment [4]. For simplicity, the time delay between the end of excitation and the beginning of acquisition is neglected, yielding [4]:

$$\alpha(N,T_2,D) = \exp\left[-(2NT/T_2 + \frac{2}{3}\gamma^2 G^2 N^3 T^3 D)\right].$$

The factor β incorporates the application of the BURST excitation [4]. The ideal flip angle of each sub-pulse in the BURST excitation approximates β for large N [4]:

$$\beta(N) \approx \frac{\pi}{2\sqrt{N}}.$$

Since the object is homogeneous and covers a large portion of the field of view in the phase encoding direction, the signal data set will form a sinc function with a sharp maximum at the center of k-space. By neglecting the contribution to the SNR of all the lines of k-space but the central line, the expression for the SNR is [4]:

$$SNR = \beta(N) \cdot \frac{1}{\sqrt{N}} \cdot \alpha(N,T_2,D).$$

Although this is a simplified case, the conclusion that the SNR decreases rapidly with increasing N is valid for the BURST approach in general. Thus, a high-resolution image will suffer significantly from poor signal quality. On the other hand, reducing resolution somewhat defeats the purpose.

VITA

MARK CHRISTIAN KREMKUS

PERMANENT ADDRESS | P.O. Box 1304
San Marcos, TX 78667

EDUCATION	Texas A&M University, College Station, TX
	B.S. Electrical Engineering as of May 11, 2001
HONORS	President's Endowed Scholarship
	National Merit Scholarship
	International Education Fee Scholarship
	Engineering Scholars Program
	Phi Kappa Phi
	National Dean's List
ACADEMIC INTERESTS	Vector Calculus
	Electromagnetics and Optics
	MRI
	Mathematical Modeling and Programming
	Graphics Programming
	Cognitive Psychology
GENERAL INTERESTS	Sailing
	Landscape and Seascape Painting